Journal of Thermal Analysis and Calorimetry (2025) 150:9039–9052
https://doi.org/10.1007/s10973-025-14338-x

Thermal decomposition of sol–gel synthesized bismuth citrate

Darren Fynn[1,2] · **Caren Billing**[1,2] · **David Gordon Billing**[1,2]

Received: 22 November 2024 / Accepted: 22 April 2025 / Published online: 24 May 2025

Abstract
This paper investigates the thermal decomposition of bismuth citrate sol–gel precursors using thermogravimetry, derivative thermogravimetry and differential thermal analysis, as well as Fourier transform infrared spectroscopy and powder X-ray diffraction with Rietveld refinement analysis. Citric acid effectively complexes Bi^{3+} to form bismuth citrate monohydrate after drying at 100 °C. Upon further heating, dehydration and decomposition of excess citric acid occurs, followed by the decomposition of bismuth citrate to form a mixture of α-Bi_2O_3 and bismuth oxide acetate at ~ 300 °C. An intermediate bismuth subcarbonate phase was detected upon further heating before final decomposition to Bi_2O_3. The subcarbonate phase has not been reported in bismuth citrate decomposition studies before. A partial phase transition from α-Bi_2O_3 to γ-Bi_2O_3 was also observed after heating to 700 °C and 750 °C.

Keywords Sol–gel · Thermal decomposition · Rietveld refinement · Bismuth oxide (Bi_2O_3) · Bismuth citrate

Introduction

Bismuth oxide (Bi_2O_3) is a pale-yellow ceramic material with a range of interesting properties that make it a suitable candidate for various applications, including photocatalysis [1, 2], gas sensing [3, 4], and solid oxide fuel cells [5–8]. These properties are due to the unique polymorphism of Bi_2O_3. α-Bi_2O_3 (space group 14, $P2_1/c$) is thermodynamically stable at room temperature [9, 10] and is an effective photocatalyst for the degradation of pollutants such as dyes, pesticides and toxins [11, 12]. α-Bi_2O_3 undergoes a phase transition to δ-Bi_2O_3 (space group 225, Fm-3m) at 729–730 °C. δ-Bi_2O_3 is thermodynamically stable at high-temperature but only in a narrow temperature range as it melts at 824–825 °C [5–7]. δ-Bi_2O_3 has the highest ionic conductivity amongst the solid oxide ion conductors, hence it has been the subject of extensive research for application as a solid oxide fuel cell electrolyte [5–8]. δ-Bi_2O_3 is unstable below 730 °C and transforms to β-Bi_2O_3 (space group 114, P-42_1c) at 650 °C or to γ-Bi_2O_3 (space group 197, I23) at 639 °C, depending on the cooling conditions. β- and γ-Bi_2O_3 then transform to α-Bi_2O_3 between 650 and 500 °C, although γ-Bi_2O_3 may often persist to room temperature [9, 10, 13]. Both β- and γ-Bi_2O_3 are more effective as photocatalysts than α-Bi_2O_3 [14–17].

Metal oxide powders (including Bi_2O_3) can be synthesized from solution-state precursors using a sol–gel method. Citric acid ($C_6H_8O_7$) is a popular small organic molecule in sol–gel chemistry due to its affordability, availability, and effectiveness as a chelating agent. When citric acid is used, the synthesis is specifically referred to as the citric acid or citrate sol–gel method [18]. The citrate sol–gel method has been used for the synthesis of Bi_2O_3 [19–23]. However, there is a lack of consistency regarding the thermal decomposition products of the bismuth citrate precursor, possibly due to deviations in experimental conditions.

Astuti et al. [22] synthesized Bi_2O_3 nano-powders using the citrate sol–gel method by incorporating polyethylene glycol (PEG) after chelating the bismuth cations with citrate. They initially found a mixture of α and γ phases, at room temperature, after annealing at temperatures of 500 °C, 600 °C, and 700 °C. However, they later found only α-Bi_2O_3 after annealing at 700 °C but after annealing at 500 °C and 600 °C they found mixtures of α-Bi_2O_3, γ-Bi_2O_3 as well as bismuth(II) monoxide (BiO) [23]. In contrast, Anilkumar et al. [21] found only β-Bi_2O_3 at room temperature after annealing at 400 °C, while Mansour [24] found

✉ Caren Billing
caren.billing@wits.ac.za

[1] Molecular Science Institute, School of Chemistry, University of the Witwatersrand, Johannesburg, South Africa

[2] DSI-NRF Centre of Excellence in Strong Materials, University of the Witwatersrand, Johannesburg, South Africa

a mixture of α- and β-Bi_2O_3 phases after annealing at 470 °C. Although γ-Bi_2O_3 is known to persist to room temperature, the reported formation temperatures of both γ- and β-Bi_2O_3 phases seem to suggest direct phase transitions from α-Bi_2O_3, and the persistence of β-Bi_2O_3 to room temperature also contradicts previous reports regarding Bi_2O_3 polymorphism [9, 10, 13]. These discrepancies warrant further investigation into the transformation mechanisms and stability of Bi_2O_3 phases synthesized using the citrate sol–gel method.

Notably, the above research primarily focuses on the final oxide phases, overlooking key information about the initial bismuth citrate ($BiC_6H_5O_7$) complex precursor [19, 20]. $BiC_6H_5O_7$ is a commonly used drug in the treatment of peptic ulcers due to its activity against *Helicobacter pylori* [25, 26]. Several studies have investigated the thermal decomposition process of $BiC_6H_5O_7$ [19, 20, 24], but there is variability in the reported temperature ranges and decomposition products formed. Notably, all these studies used a heating rate of 10 °C min^{-1} in air. Radecki and Wesołowski [19] suggested that dehydration of $BiC_6H_5O_7{\cdot}2H_2O$ (dihydrate) begins at 80 °C and ends by 200 °C. Srivastava et al. [20], who synthesised $BiC_6H_5O_7$ by precipitation with sodium citrate, observed dehydration of $BiC_6H_5O_7{\cdot}H_2O$ (monohydrate) occurring in a wider range from 39 to 225 °C. They further suggest partial decomposition of $BiC_6H_5O_7$ by 332 °C, giving a mixture of Bi_2O_3 and bismuth oxide acetate ($BiOC_2H_3O_2$, BiOAc), with a 1:3 (Bi_2O_3:BiOAc) molar ratio. Mansour [24], who analysed purchased $BiC_6H_5O_7$, proposed that partial decomposition of anhydrous $BiC_6H_5O_7$ gives a mixture of Bi_2O_3, BiOAc, and BiO, with a 1:1:1 molar ratio, by 325 °C. BiOAc then decomposes further to form Bi_2O_3 by 400 °C (according to Mansour [24]) or by 410 °C (according to Srivastava et al. [20]). According to Mansour [24], BiO undergoes oxidation to form Bi_2O_3 up to 850 °C, but this is above the melting point of Bi_2O_3 [6–9]. In contrast, Radecki and Wesołowski [19] reported largely a single-step decomposition of $BiC_6H_5O_7$ to Bi_2O_3 by 470 °C.

The contrasting findings in literature regarding the formation of Bi_2O_3 through the thermal decomposition of $BiC_6H_5O_7$ warrants further investigation to provide a more comprehensive understanding of the process. In the present work, we address this by investigating the thermal decomposition of $BiC_6H_5O_7$ precursors prepared using the citric acid sol–gel method. The thermal decomposition pathway of the $BiC_6H_5O_7$ precursors is probed using differential thermal analysis (DTA), thermogravimetry (TG) and derivative thermogravimetry (DTG). The decomposition products are identified using Fourier transform infrared (FTIR) spectroscopy and powder X-ray diffraction (XRD) followed by quantitative Rietveld refinement [27] of the XRD patterns.

Experimental

Sample preparation

All samples were synthesised using a citric acid sol–gel method. Bismuth (III) nitrate pentahydrate ($Bi(NO_3)_3{\cdot}5H_2O$, 99.99% pure, Sigma-Aldrich) was dissolved in glacial acetic acid (98% pure, MK Chemical) under mild heat and constant stirring. Citric acid monohydrate ($C_6H_8O_7{\cdot}H_2O$, ACS reagent, Sigma-Aldrich) was then added such that the molar ratio of Bi^{3+}:citric acid was 1:1 (BiCit1), 1:2 (BiCit2), and 1:3 (BiCit3), respectively. The glacial acetic acid (boiling point: 118 °C [28]) was subsequently evaporated and the nitrates decomposed to form nitrogen dioxide (NO_2), observed by its distinctive reddish-brown colour [29], and oxygen. The white gel that remained was oven-dried overnight at 100 °C and then at 200 °C, with analysis of the residues after each step. BiCit3 samples were also annealed further in a calibrated Lenton chamber furnace between 300 and 700 °C in 100 °C intervals for two hours (at each temperature), and then finally at 750 °C. A heating rate of 10 °C min^{-1} was used, and the samples were left to cool to room temperature in the furnace.

Sample characterisation

All FTIR and XRD measurements were performed under ambient conditions. FTIR spectra were measured using a Bruker ALPHA II FTIR spectrometer equipped with a ZnSe crystal as part of the Eco-ATR sampling module. FTIR spectra were measured from 600 to 4000 cm^{-1} at a resolution 4 cm^{-1} with 24 scans per sample, and background noise was subtracted.

Powder XRD patterns were measured using a Bruker AXS D2 PHASER desktop diffractometer. The instrument was equipped with a sealed tube Co $K_{\alpha1}/K_{\alpha2}$ X-ray source (30 kV, 10 mA) with $\lambda = 1.78900/1.79283$ Å, a 0.6 mm fixed divergent slit, 2.5° primary and secondary beam Söller slits, an iron filter to attenuate K_β radiation, and a Lynxeye linear position sensitive detector with an effective angular range of 5° 2θ. The instrument was calibrated using NIST SRM 660c (LaB6, lanthanum hexaboride) and the instrumental resolution function was determined using the extended Thompson-Cox-Hastings pseudo-Voigt (TCHZ) approach as outlined by Dinnebier et al. [30]. XRD patterns were measured between 5 to 100° 2θ using a step size of 0.026° 2θ. For all the XRD patterns presented here, the crystalline phase identification and quantification was determined using the Rietveld method [27] as implemented in the Bruker AXS TOPAS software (Version 7).

The thermal decomposition of the samples oven-dried at 100 °C (BiCit*n*-100, where $n = 1–3$) as well as the BiCit3 sample dried at 200 °C (BiCit3-200) was investigated through simultaneous TG and DTA using a PerkinElmer STA600 with a heating rate of 10 °C min^{-1} in an atmosphere of technical grade air (African Oxygen Limited) flowing at a rate of 20 mL min^{-1}. Thermal analysis data acquisition as well as data processing and analysis were performed using PerkinElmer's Pyris software. For the residual mass analysis of the TG curves, the molecular masses used in the theoretical calculations are according to the International Union of Pure and Applied Chemistry (IUPAC) [31].

Results and discussion

Characterisation of bismuth citrate precursors using FTIR spectroscopy and XRD

The ambient XRD pattern of citric acid (black), which was treated the same as the other samples by dissolving in acetic acid followed by oven drying at 100 °C, is shown in Fig. 1a. According to Lafontaine et al. [32] this represents the anhydrous form of citric acid. XRD patterns of BiCit1 (blue), BiCit2 (grey), and BiCit3 (red) oven-dried at 100 °C (Fig. 1a) are significantly different compared to that of citric acid, which supports the effective complexation of Bi^{3+} by citrate during the sample synthesis. For BiCit2-100 and BiCit3-100, peaks at ~ 16°, 21°, 23°, 28° and 30° 2θ show a noticeable growth in the intensity, indicated by ∇ in Fig. 1a. These peaks are not distinct in the XRD pattern of BiCit1-100. Since the relative intensity of these peaks increase from BiCit2-100 to BiCit3-100, it is proposed that they correspond to an increase in excess uncomplexed citric acid with increased amount of citric acid added, which is consistent with the formation of bismuth citrate complexes with an overall Bi^{3+}:citrate ratio of 1:1. Given the established ability of Bi^{3+} to form complexes with high coordination numbers (ranging from three to ten), coupled with the variability in its coordination geometries [33], it was important to confirm a Bi^{3+}:citrate ratio of 1:1. The dominance of the bismuth citrate diffraction pattern even in the presence of two times more citric acid (BiCit3-100) is due to the significantly higher scattering factor of Bi^{3+} ions [34].

The samples oven-dried at 100 °C overnight were initially more white in colour (Fig. 1b), but after oven-drying at 200 °C, they were brown in colour (Fig. 1c). Despite the noticeably different visual appearance of the samples, there is a high degree of similarity between the XRD patterns (Fig. 1a) for BiCit3-100 (red) and BiCit3-200 (orange), which suggests that the $BiC_6H_5O_7$ crystal structure is maintained after oven-drying at 200 °C. However, in the BiCit3-200 XRD pattern the peaks at 23° and 30° 2θ were no longer

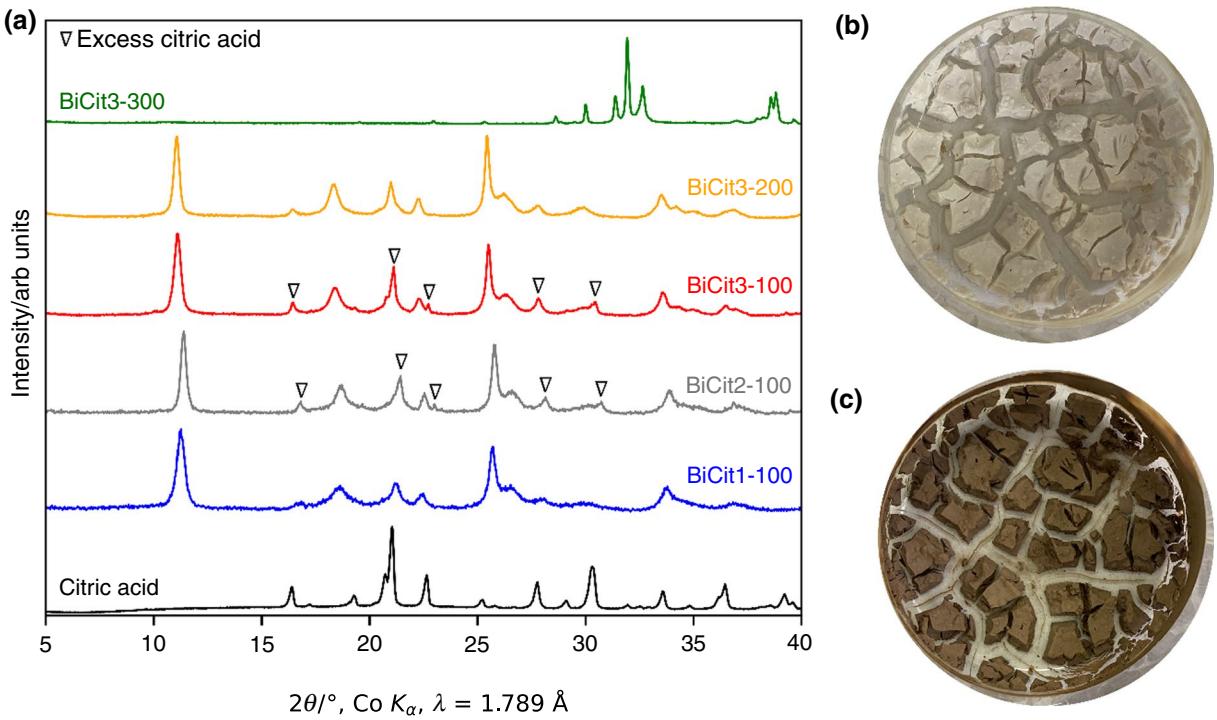

Fig. 1 **a** XRD patterns of the $BiC_6H_5O_7$ sol–gel precursors and citric acid. **b** BiCit3 after oven-drying at 100 °C overnight, and **c** BiCit3 after oven-drying at 200 °C overnight

observed, while the peaks at 16°, 21° and 28° 2θ decreased in intensity (more similar to BiCit1-100), which suggests the thermal decomposition of excess citric acid during oven-drying at 200 °C. In contrast, the XRD pattern of BiCit3-300 (green) is significantly different compared to BiCit3-100 and BiCit3-200, indicating the complete thermal decomposition of the $BiC_6H_5O_7$ complex during heating at 300 °C for two hours.

These samples were also analysed using FTIR spectroscopy and the room temperature spectra are shown in Fig. 2a. The spectrum for citric acid (black) has a sharp absorption band at ~ 3500 cm^{-1}, along with a broader absorption band centred at ~ 3280 cm^{-1}, which are due to O–H stretching vibrations within the carboxylic acid groups (indicated by * in Fig. 2a, b) [35–37]. A less intense absorption band observed at ~ 3450 cm^{-1} can be assigned to the O–H stretching vibration of the tertiary alcohol group (indicated by + in Fig. 2a, b) [35]. The weak absorption bands in the region between 2900 and 3000 cm^{-1} correspond to C–H stretching vibrations of the methylene (CH_2) groups (indicated by ^ in Fig. 2a, b). Two prominent absorption bands in the range of 1700–1800 cm^{-1} correspond to carbonyl (C=O) stretching vibrations (indicated by ∇ in Fig. 2a, b) [35–37]. The absorption bands observed between 1200 and 1300 cm^{-1} correspond to C–O stretching vibrations (marked with ↓ in Fig. 2a, b) [35–37]. These assignments are summarised in Table 1.

The FTIR spectra of both BiCit2-100 (grey) and BiCit3-100 (red) (Fig. 2a) display the characteristic citric acid absorption bands for the carboxyl O–H stretching (*), C=O stretching (∇) and C–O stretching (↓), but these bands are absent from the spectrum for BiCit1-100 (blue). The absence of the characteristic carboxyl O–H stretching bands (*) in BiCit1-100 suggests the deprotonation of the carboxylic acid

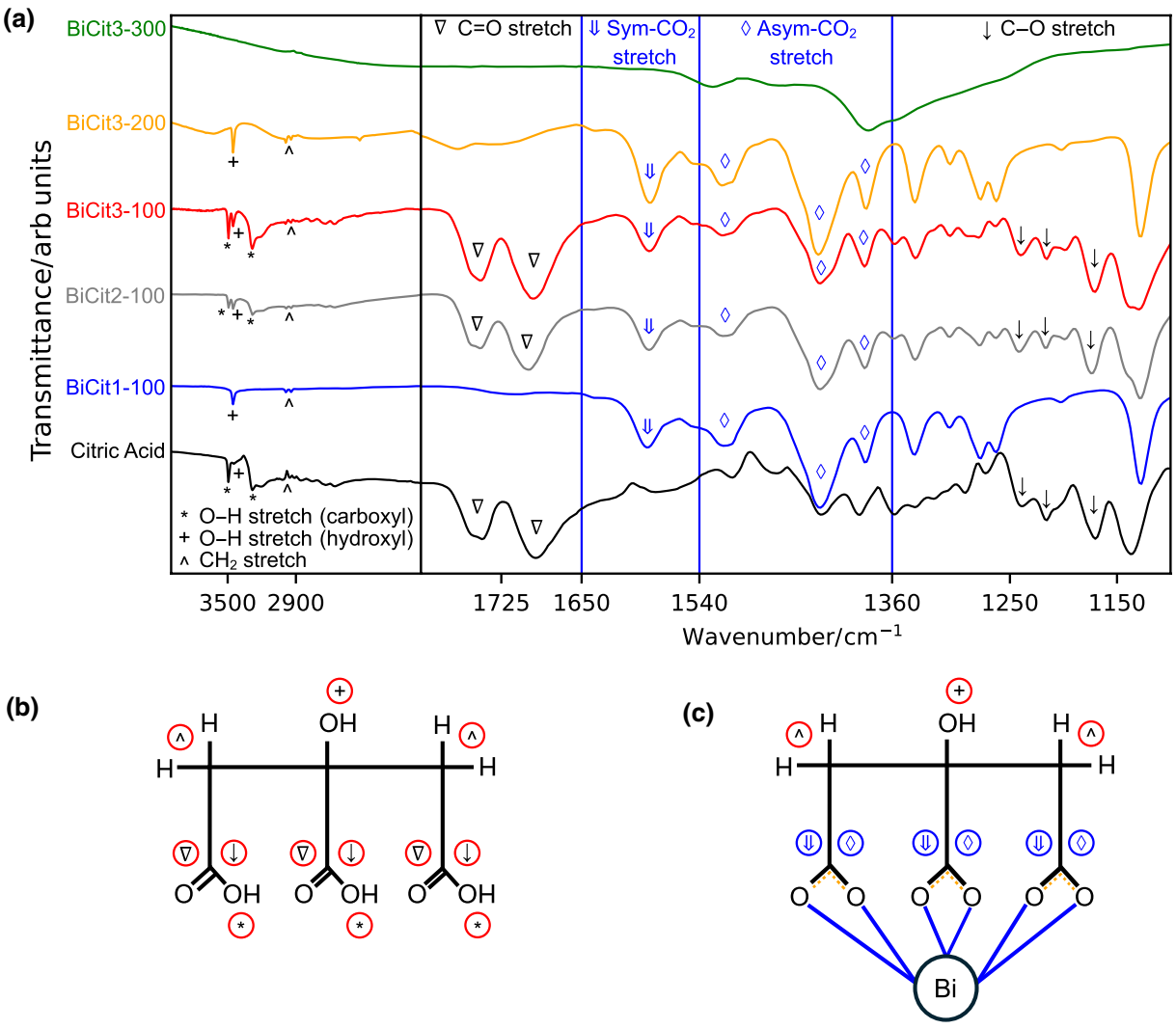

Fig. 2 **a** FTIR spectra of the $BiC_6H_5O_7$ sol–gel precursors and citric acid. Skeletal formulae of **b** anhydrous citric acid, and **c** $BiC_6H_5O_7$, highlighting the functional groups responsible for the stretching vibrations observed in the spectra

Table 1 Assignment of the characteristic absorption bands in the FTIR spectrum of citric acid in Fig. 2a

Wavenumber range/cm^{-1}	Relative intensity	Assignment	Symbol
3500 and 3280	Medium	Carboxyl O–H stretch	*
3450	Weak	Hydroxyl O–H stretch	+
2900–3000	Very Weak	CH_2 stretch	^
1700–1800	Strong	C=O stretch	∇
1200–1300	Strong	C–O stretch	↓

Table 2 Assignment of the characteristic absorption bands in the FTIR spectrum of BiCit1-100 in Fig. 2a

Wavenumber range/cm^{-1}	Relative intensity	Assignment	Symbol
3450	Weak	Hydroxyl O–H stretch	+
2900–3000	Very Weak	CH_2 stretch	^
1650–1560	Strong	Asymmetric CO_2 stretch	⇓
1540–1360	Strong	Symmetric CO_2 stretch	⋄

groups when forming the $BiC_6H_5O_7$ complex. Additionally, the lack of the characteristic C=O stretching absorption bands (∇) is due to the delocalisation of electrons across the two C–O bonds in the carboxylate groups when deprotonated (represented by orange lines in Fig. 2c). When complexation between Bi^{3+} and the carboxylate groups occur, the symmetric and asymmetric CO_2 stretching bands (typically around 1450–1360 cm^{-1} and 1650–1540 cm^{-1}, respectively [37]) are more pronounced. Since these vibrations involve the carbon and both oxygens, they are referred to as "CO_2" stretching vibrations as indicated in Fig. 2a (⇓). The persistence of the hydroxyl O–H stretching band due to the tertiary alcohol group (+) in the BiCit1-100 spectrum shows that this functional group does not participate in the complexation of Bi^{3+}, as indicated in Fig. 2c. The assignments for the spectrum for BiCit1-100 are summarised in Table 2. These results suggest that excess citric acid is present in BiCit2-100 and BiCit3-100, but not BiCit1-100, which again is consistent with the formation of a complex with a Bi^{3+}:citrate ratio of 1:1.

The spectrum for BiCit3-200 (orange) is more comparable to that for BiCit1-100, showing that decomposition of excess citric acid occurs during oven-drying at 200 °C. The FTIR spectrum of BiCit3-300 (green) is significantly different compared to the spectra of all other samples analysed. This suggests the complete thermal decomposition of the citrate complex ($BiC_6H_5O_7$) by 300 °C. These results all align with the conclusions drawn from the XRD analysis.

Qualitative analysis of the BiCit3-300 XRD pattern (Fig. 3a) indicates the clear presence of α-Bi_2O_3 ($P2_1/c$, ICSD card no. 2374) [9], together with an additional phase (most likely a minor phase due to the lower intensity peaks). Previous studies suggested the formation of BiOAc during bismuth citrate thermal decomposition [20, 24], but the formation of BiOAc was only inferred using thermogravimetry. Unfortunately, the crystal structure for BiOAc has not been reported in established crystallographic databases, but previous literature suggests BiOAc is isostructural with the bismuth oxide halide crystal structures (BiOCl - ICSD card no. 24608, BiOBr - ICSD card no. 24609 and BiOI - ICSD card no. 24610). These have P4/nmm space group symmetry, as well as similar Bi^{3+}, O^{2-} and halide crystallographic positions [38, 39]. The BiOAc crystal structure is described as also having P4/nmm space group symmetry with similar Bi^{3+} and O^{2-} crystallographic positions which form a $Bi_2O_2^{2+}$ layer, but with acetate replacing the halides which form a double interlayer (see Fig. S2.1 and corresponding crystallographic data in Table S2.1–2.3.) [38].

Assuming a P4/nmm space group for BiOAc, the additional minor phase reflections were indexed (shown as orange * in Fig. 3a and are indexed in Table S1) and include (101) at 32.5° 2θ, (002) at 37° 2θ, (110) at 38° 2θ, (200) at 55° 2θ, and (103) at 64° 2θ. The most intense (101) BiOAc reflection overlaps with the (012) reflection of α-Bi_2O_3, causing a noticeable asymmetry in the combined peak profile. Rietveld refinements were done with respect to the diffraction patterns in Fig. 3a, b using the BiOCl structure (P4nmm space group) as the starting model. The refined *c*-axis length of BiOAc (~ 5.65 Å) is significantly smaller than that for the bismuth oxide halides (7.347 Å for BiOCl, 8.092 Å for BiOBr, and 9.128 Å for BiOI), while the refined length of the *a*-axis of BiOAc (~ 3.87 Å) and the bismuth oxide halides (3.883–3.984 Å) are well aligned. This suggests a preferential orientation of the approximately trigonal planar acetate ions along the *c*-axis direction [39].

Although the absence of a BiOAc crystal structure prevents accurate quantification using Rietveld refinement, alternative strategies were explored to estimate of the BiOAc concentration, as this may provide important insights into the thermal decomposition of bismuth citrate. The bismuth

oxide halides were thus used as proxies for BiOAc in the Rietveld refinements due to their reported structural similarity, and since a large contribution of the diffracted intensity is due to the significantly heavier Bi^{3+} ions [34, 38]. While this is not a commonly applied procedure, it highlighted the significant intensity difference between the major α-Bi_2O_3 and minor BiOAc phases (Fig. 3a), and produced a good fit for the minor phase, suggesting a reasonable approximation of the P4/nmm space group symmetry and the Bi^{3+} crystallographic positions. It should be noted that the different electron counts for the anions (32 for acetate, 18 for Cl^-, 36 for Br^-, and 53 for I^-) and their molar masses (59.0 for acetate, 35.5 for Cl^-, 79.9 for Br^-, and 126.9 for I^-), among others, introduce error in the quantification by affecting the scattering factor and mass % calculation. Consequently, the true concentration of BiOAc in BiCit3-300 should fall within the range defined by the concentrations estimated using BiOI (18 mass% at 300 °C) and BiOCl (31 mass% at 300 °C) as structural proxies. All the results of the quantitative phase analysis from the Rietveld refinement of BiCit3 (annealed at different temperatures) are summarized in Table 3.

It is important to note that the approximate concentrations estimated from the Rietveld refinements using the bismuth oxide halides as structural proxies are sensitive to the scattering power of the crystal structure model used. Specifically, the use of the iodide ion, characterized by a much higher electron count (54 electrons) compared to the acetate ion (32 electrons) and consequently stronger X-ray scattering, may result in an underestimation of the true BiOAc concentration compared to the hypothetical use of an accurate BiOAc crystal structure, despite the fact that the majority of the diffracted intensity is contributed by the significantly heavier and electron-rich Bi^{3+} ions. Conversely, using the chloride ion, with a much lower electron count (18 electrons) compared to acetate and consequently weaker X-ray scattering, could lead to an overestimation of the true BiOAc concentration relative to the hypothetical scenario where the BiOAc crystal structure is available [30, 34]. Consequently, the true concentration of BiOAc in BiCit3-300 may fall within the range defined by the approximate concentrations estimated using BiOI (18 mass%) and BiOCl (31 mass%) as structural proxies. The results of the quantitative phase analysis from the Rietveld refinement of BiCit3 (annealed at different temperatures) are summarized in Table 3. The crystal structure of the bismuth oxide halides is shown in Fig. S2.1, with the corresponding crystallographic data in Tables S2.1–2.3.

The XRD analysis therefore suggests the complete decomposition of $BiC_6H_5O_7$ after annealing at 300 °C for 2 h. In contrast to the decomposition products reported by Mansour [24] (which included BiO alongside α-Bi_2O_3 and

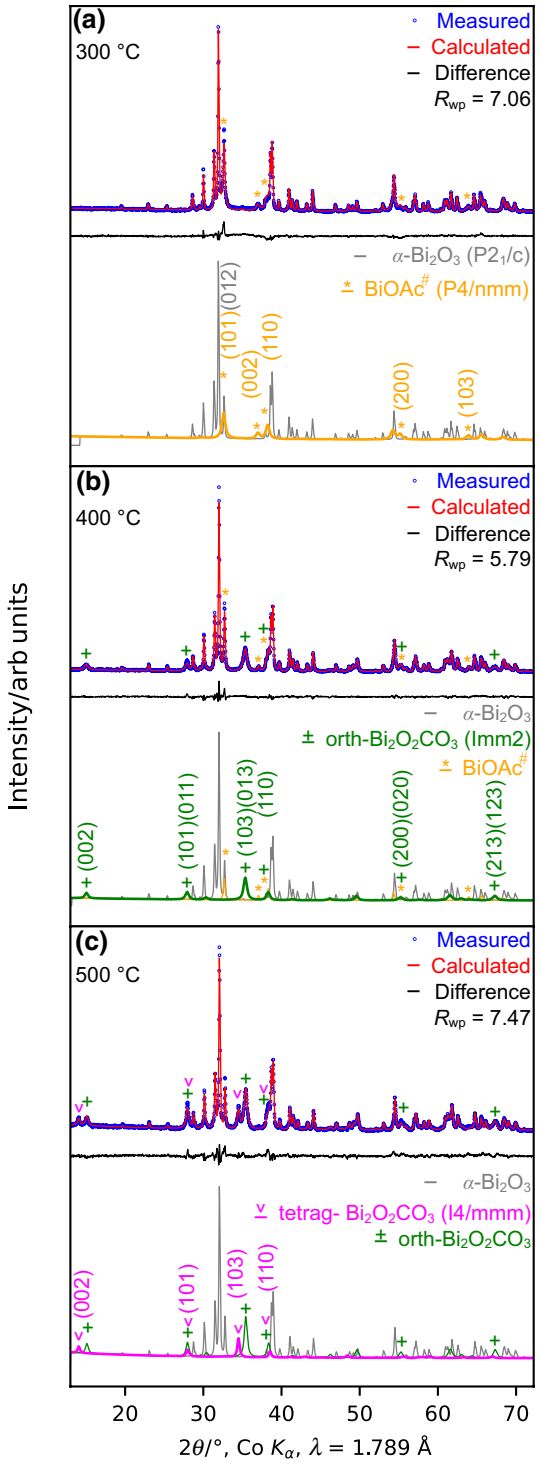

Fig. 3 Rietveld refinement of the XRD patterns of BiCit3 annealed at different temperatures: **a** BiCit3-300, **b** BiCit3-400, and **c** BiCit3-500. The measured patterns (blue) were refined using a mixture of phases, including α-Bi_2O_3 (grey), BiOAc# (*, orange), orthorhombic $Bi_2O_2CO_3$ (+, green), and tetragonal $Bi_2O_2CO_3$ (v, magenta). #The bismuth oxide halides (BiOCl, BiOBr or BiOI) were used as proxies for BiOAc due to their structural similarity [38]

Table 3 Quantitative phase analysis determined from the Rietveld refinement of XRD patterns for BiCit3 after annealing for two hours at each temperature

Annealing Temperature/°C	Phase/mass%				
	α-Bi_2O_3	BiOAc[#]	*orth*-$Bi_2O_2CO_3$	*tetrag*-$Bi_2O_2CO_3$	γ-Bi_2O_3
300	69[a], 74[b], 82[c]	31[a], 26[b], 18[c]	–	–	–
400	68[a], 69[b], 71[c]	10[a,b], 7[c]	22[a,c], 21[b]	–	–
500	58	–	27	15	–
600	100	–	–	–	–
700	94	–	–	–	6
750	95	–	–	–	5

[#]Bismuth oxide halides ([a]BiOCl, [b]BiOBr or [c]BiOI) were used as proxies for BiOAc due to their structural similarity [38]

BiOAc), no reflections due to BiO were observed in the XRD patterns presented throughout this study. While BiO is known to exist in the gas phase [28], its existence in the solid state is uncommon. The 2+ oxidation state of bismuth is extremely rare, making solid BiO an unusual, unstable and not a frequently reported oxide of bismuth [28, 40, 41]. The absence of BiO reflections in the XRD patterns is therefore not surprising especially when annealing occurs in air. Therefore, based on the XRD analysis of BiCit3-300, the thermal decomposition of $BiC_6H_5O_7$ results in a two-phase mixture consisting of α-Bi_2O_3 and BiOAc. This agrees with the thermal decomposition step reported by Srivastava et al. [20].

Rietveld refinement of the BiCit3-400 XRD pattern (Fig. 3b) revealed a three-phase mixture consisting of α-Bi_2O_3, orthorhombic bismuth subcarbonate (*orth*-$Bi_2O_2CO_3$; Imm2, ICSD no. 94740) [42] (indicated by green + in Fig. 3b) as well as the bismuth oxide halide-type BiOAc phase. As before, the bismuth oxide halide crystal structures were used as proxies for BiOAc to estimate the concentrations of BiOAc from the quantitative phase analysis, which showed a notable decrease in the BiOAc concentration compared to BiCit3-300 (Table 3). This, together with the emergence of *orth*-$Bi_2O_2CO_3$ suggests that the thermal decomposition of BiOAc leads to the formation of *orth*-$Bi_2O_2CO_3$. In the BiCit3-400 XRD pattern, the most intense peak associated with *orth*-$Bi_2O_2CO_3$ is at 35° 2θ and is due to (103) and (013) reflections. Additional prominent peaks of *orth*-$Bi_2O_2CO_3$ are observed at 15° 2θ for the (002) reflection, and at 28° 2θ due to (101) and (011) reflections. A complete list of bismuth oxide halide-type BiOAc and *orth*-$Bi_2O_2CO_3$ reflections identified in the BiCit3-400 XRD pattern are given in Table S1. The refined crystal structure of *orth*-$Bi_2O_2CO_3$ is shown in Fig. S3.1, with the crystallographic data in Table S3.1.

Rietveld refinement of the BiCit3-500 XRD pattern (Fig. 3c) reveals the absence of the bismuth oxide halide-type BiOAc phase. The measured pattern can be described by a three-phase mixture consisting of α-Bi_2O_3, *orth*-$Bi_2O_2CO_3$, and a newly formed tetragonal $Bi_2O_2CO_3$ phase (*tetrag*-$Bi_2O_2CO_3$; I4/mmm, ICSD no. 36245) [43] (indicated by magenta ∨ in Fig. 3c). The quantitative phase analysis results (Table 3) show a significant increase in the estimated concentration of $Bi_2O_2CO_3$ in BiCit3-500 compared to BiCit3-400. Some of the increase in *orth*-$Bi_2O_2CO_3$ will likely be due to the decomposition of the remaining BiOAc, however, this cannot account for the entire increase in concentration and for the emergence of *tetrag*-$Bi_2O_2CO_3$. An additional source of carbon is necessary to explain the increase in $Bi_2O_2CO_3$. Although the actual source of the additional carbon is not known at this stage, a potential source is likely from the excess uncomplexed citric acid. Citric acid does not fully decompose below 500 °C (see Fig. S6) but rather partially decomposes and forms intermediates like aconitic acid ($C_6H_6O_6$) or methyl maleic anhydride ($C_5H_4O_3$) [44]. The CO_2 released from the thermal decomposition of these intermediates may provide the additional carbon necessary for $Bi_2O_2CO_3$ formation. This was shown to be possible in a hydrothermal synthesis where the decomposition of urea provided the CO_2 necessary for $Bi_2O_2CO_3$ formation from Bi_2WO_6 [19]. Additionally, in the thermal analysis of bismuth citrate, an amorphous coked residue was shown to form between 300 and 350 °C [45]. At higher temperatures this could possibly be oxidised to provide the CO_2 needed for $Bi_2O_2CO_3$ formation.

orth-$Bi_2O_2CO_3$ is likely more thermodynamically stable at room temperature due to its lower symmetry compared to *tetrag*-$Bi_2O_2CO_3$. *tetrag*-$Bi_2O_2CO_3$ is probably metastable and persists to room temperature, similar to the behaviour observed for γ-Bi_2O_3 [9, 10, 13] or the metastable aragonite polymorph of calcium carbonate ($CaCO_3$) [46]. The most prominent reflection of *tetrag*-$Bi_2O_2CO_3$, in the BiCit3-500 XRD pattern, is the (103) reflection at 34.5° 2θ and an additional notable reflection is the (002) reflection at 14° 2θ. A complete list of *tetrag*-$Bi_2O_2CO_3$ and *orth*-$Bi_2O_2CO_3$ reflections identified in the BiCit3-500 XRD pattern is provided in Table S1. An interesting observation is the visual similarity of the XRD patterns for *tetrag*-$Bi_2O_2CO_3$ and

orth-$Bi_2O_2CO_3$. This is most apparent when comparing the (103) reflection and the (002) reflection, which have similar positions and relative intensities in the two phases, although they are shifted towards lower 2θ angles for *tetrag*-$Bi_2O_2CO_3$. This suggests a high degree of structural similarity between the two phases, and this is further supported by visually comparing the refined crystal structures of *orth*-$Bi_2O_2CO_3$ (Fig. S2) and *tetrag*-$Bi_2O_2CO_3$ (Fig. S3.2). The refined crystallographic data for *tetrag*-$Bi_2O_2CO_3$ is given in Table S3.2.

The $Bi_2O_2CO_3$ phases (both *orth* and *tetrag*) are no longer observed in the XRD patterns for BiCit3 when annealed at 600 °C and above (Fig. 4), indicating thermal decomposition of $Bi_2O_2CO_3$ occurs between 500 and 600 °C. Rietveld refinement of the XRD pattern for BiCit3-600 (Fig. 4a) shows all reflections can be solely attributed to α-Bi_2O_3. The refined crystal structure of the resulting α-Bi_2O_3 phase is shown in Fig. S4, with the crystallographic data given in Table S4.

The Rietveld refinement of the XRD patterns for BiCit3-700 and BiCit3-750 (Fig. 4b, c) reveals α-Bi_2O_3 as the major phase, however, several additional peaks are also present. The most prominent of these is located at 32.75° 2θ, situated between the (120) and (012) reflections of α-Bi_2O_3. This reflection can be assigned to the (301) and (310) reflections of γ-Bi_2O_3 (I23, ICSD card no. 2376) [9] (indicated by sky blue ∇ in Fig. 4b). Another significant peak at 36° 2θ corresponds to the (222) reflection of γ-Bi_2O_3. Distinguishing between β-Bi_2O_3 and γ-Bi_2O_3 solely based on the peaks at 32.75° 2θ and 36° 2θ is challenging, as these positions could also correspond to the (201) and (002) reflections of β-Bi_2O_3, respectively. Nevertheless, additional peaks at 46.75° 2θ and 51.5° 2θ are present in the XRD pattern. These peaks are absent for both α-Bi_2O_3 and β-Bi_2O_3 [9] but match the (402) and (420) reflections at 46.75° 2θ, and the (422) reflection at 51.5° 2θ for γ-Bi_2O_3, therefore confirming its formation. The results of the quantitative phase analyses from the Rietveld refinements of BiCit3-700 and BiCit3-750 are summarized in Table 3.

Although γ-Bi_2O_3 is known to be metastable and could persist to room temperature, its presence in BiCit3-700 is notable, as previous reports suggest that the formation of γ-Bi_2O_3 proceeds through a δ-to-γ transition upon cooling [9, 10, 13]. Since a temperature of 700 °C is not sufficient for the α-to-δ phase transition in Bi_2O_3 to occur, the identification of some γ-Bi_2O_3 together with α-Bi_2O_3 for BiCit3-700, suggests a potential direct phase transition from α-Bi_2O_3 to γ-Bi_2O_3 at this lower temperature. Astuti et al. [22, 23] also found a mixture of α and γ phases at room temperature after annealing nanoparticles at 500 °C and 600 °C. However, this

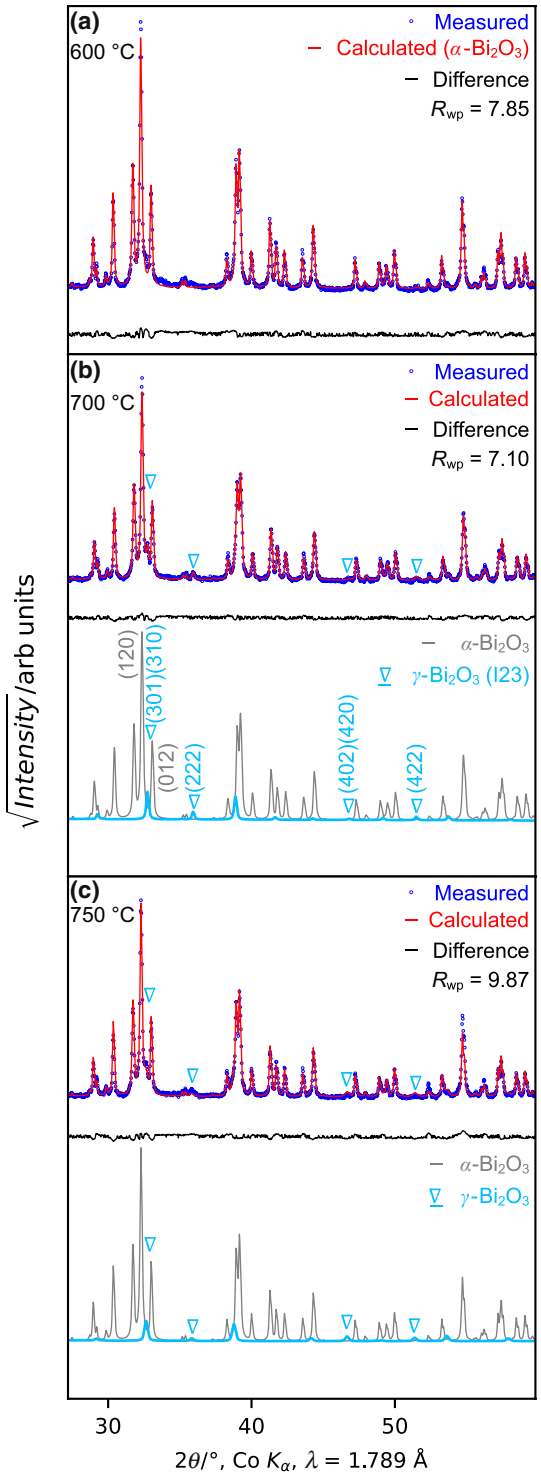

Fig. 4 Rietveld refinement of the XRD patters of BiCit3 annealed at different temperatures: **a** BiCit3-600, **b** BiCit3-700, and **c** BiCit3-750. The measured patterns (blue) were refined using α-Bi_2O_3 (light grey) for BiCit3-600, and a mixture of α-Bi_2O_3 and γ-Bi_2O_3 (∇, sky blue) for BiCit3-700 and BiCit3-750

incidental finding can only be verified by a comprehensive *in-situ* variable temperature study of the material which is not the scope of this work. BiCit3-750 has a similar phase composition as BiCit3-700 (Table 3), but it is annealed above the α-to-δ phase transition temperature so γ-Bi_2O_3 is likely formed through the traditional γ-to-δ phase transition. The γ-Bi_2O_3 peaks identified in the XRD patterns are indicated by sky blue ∇ in Fig. 4b, c and listed in Table S1, with the refined crystal structure of γ-Bi_2O_3 shown in Fig. S5.

Thermal analysis of bismuth citrate precursors using DTA, TG and DTG

Although the ambient characterization study provides valuable insights, particularly regarding the formation and identity of the decomposition products, it limits the direct determination of the decomposition step temperatures. Additionally, the isothermal annealing steps can potentially limit the usefulness of the quantitative phase analysis to describe the actual decomposition pathway. The annealing steps may drive unintended or unwanted side reactions, which are kinetically limited, during annealing or cooling, and this can alter the final phase composition. Unlike the characterisation study discussed above, thermal analysis provides real-time insights into the thermal behaviour of these materials. Through DTA, TG, and DTG, the temperatures of the decomposition steps can be directly determined. Additionally, through residual mass analysis of TG curves, in conjunction with the complementary ambient characterization, a more comprehensive understanding of the decomposition products, and consequently the decomposition pathway, can be developed.

The XRD and FTIR spectroscopic analysis of BiCit3-100 and BiCit3-200 suggested complete thermal decomposition of excess citric acid had occurred by 200 °C. This is also observed in the thermal analysis data. The DTA curve (Fig. 5a) of citric acid (black) shows a sharp endothermic peak at ~ 150 °C (inset of Fig. 5a) followed by a broader endothermic feature spanning from ~ 165 to 240 °C. This observation aligns well with previous reports for citric acid decomposition [44, 47]. Endothermic features with a similar profile to that observed for pure citric acid are seen in the DTA curves of BiCit2-100 (grey) and BiCit3-100 (red) (Fig. 5a). Radecki and Wesołowski [19] and Srivastava et al. [20] previously attributed the endothermic features to a dehydration process. This would clearly not be the case for citric acid which was shown to be in the anhydrous form. Additionally, these endothermic features are only present for BiCit2-100 and BiCit3-100 which contain excess citric acid, and not for BiCit1-100 (blue) and BiCit3-200 (orange) which do not contain excess citric acid (Fig. 5a). This supports the thermal decomposition of excess citric acid occurring between ~ 130 and 240 °C. The very broad peak (from ~ 165 to 240 °C) may point to this being a slow process which is why annealing at 200 °C for two hours was sufficient to decompose the excess citric acid. Furthermore, the DTG curves display a peak at ~ 220 °C for citric acid (black) and BiCit3-100 (red), and at ~ 170 °C for BiCit2-100 (grey), denoted by (1) in Fig. 5b. Such a peak is absent for BiCit1-100 (blue) and BiCit3-200 (orange). With the area under the peak representing the mass loss during this thermal event, the significant area under the peak for BiCit2-100 (13.8 mass% loss) and BiCit3-100 (31.5 mass% loss) thus represents the decomposition of citric acid rather than dehydration.

The residual mass after the entire thermal cycle also provided some insight into the extent of hydration of $BiC_6H_5O_7$ after drying at 100 °C (Fig. 5c). The theoretical residual mass for the thermal decomposition of $BiC_6H_5O_7{\cdot}2H_2O$ (dihydrate) to form Bi_2O_3 is 53.7 mass%, whereas it is 56.0 mass% for $BiC_6H_5O_7{\cdot}H_2O$ (monohydrate) and 58.5 mass% for anhydrous $BiC_6H_5O_7$. The observed residual mass of 55.3 mass% for BiCit1-100 (where no excess citric acid is present) thus aligns well with the theoretical residual mass for the monohydrate. Thus, given the theoretical residual mass for $BiC_6H_5O_7{\cdot}H_2O$ after complete dehydration is 98.9 mass%, it was observed that this residual mass is attained at ~ 150 °C on the TG curve for BiCit1-100, which suggests that dehydration of BiCit1 is complete by this temperature. Notably, the dehydration process is complete just before the onset of mass loss step (1) seen in DTG curves (Fig. 5b) and the onset of the endothermic features seen in the DTA curves between ~ 130 and 240 °C for citric acid, BiCit2-100 and BiCit3-100 (Fig. 5a). This again supports that mass loss step (1) seen for BiCit2-100 and BiCit3-100 corresponds to the thermal decomposition of excess anhydrous citric acid, as dehydration would have occurred before this mass loss step. The residual mass after cooling back to room temperature as determined from the TG curves (Fig. 5c) reveals the trend where BiCit3-100 has the lowest residual mass (29.0 mass%), followed by BiCit2-100 (38.4 mass%) and BiCit-100 (55.3 mass%), showing a progressive increase in total mass loss with increasing excess citric acid content.

Hence the evidence collectively suggests that the endothermic features between ~ 130 and 240 °C seen in the DTA curves (Fig. 5a), as well as mass loss step (1) in the DTG and TG curves (Fig. 5b, c), corresponds to the thermal decomposition of excess citric acid (after the dehydration of $BiC_6H_5O_7{\cdot}H_2O$), which is in agreement with the results from the ambient characterisation discussed above and occurs according to Eq. (1).

$$BiC_6H_5O_7(s) + xC_6H_8O_7(s) + 4.5xO_2(g) \rightarrow BiC_6H_5O_7(s) + 6xCO_2(g) + 4xH_2O(g) \quad (1)$$

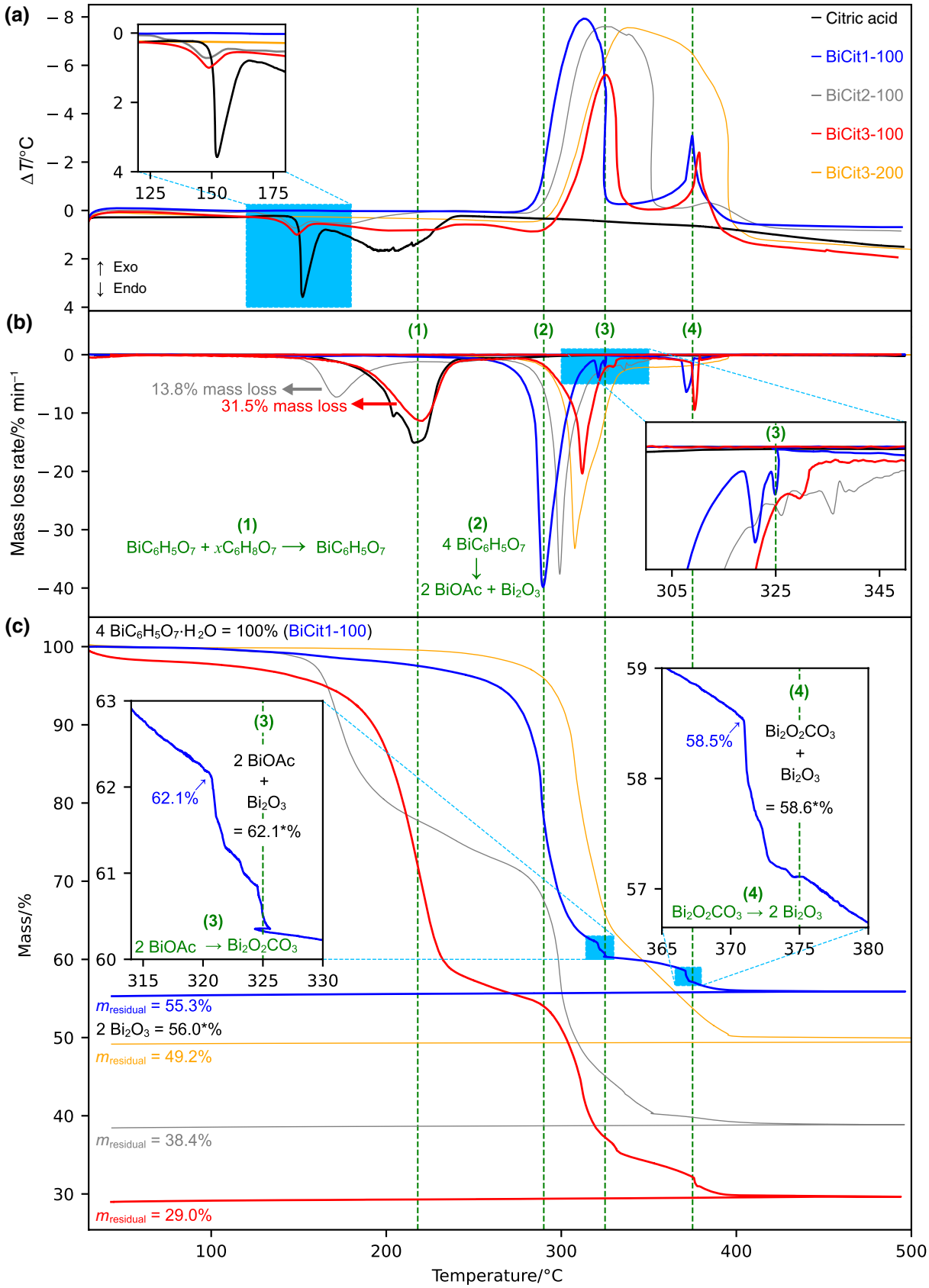

Fig. 5 Thermal analysis, including **a** DTA, **b** DTG and **c** TG curves, of citric acid and $BiC_6H_5O_7$ precursors with varying citric acid content. Theoretical residual masses were determined relative to four (4) moles of $BiC_6H_5O_7{\cdot}H_2O$ and are indicated by *

where $x = 0$ for BiCit1-100, $x = 1$ for BiCit2-100 and $x = 2$ for BiCit3-100.

Despite the observed differences in the thermal behaviour related to excess citric acid decomposition, the overall similarities in the DTA and DTG curves of all the samples above 250 °C (Fig. 5a, b) suggest a shared pathway for the main decomposition of $BiC_6H_5O_7$. The DTA curves for BiCit1, BiCit2, and BiCit3-100 (Fig. 5a) all have two distinct exothermic peaks—a prominent peak at ~ 310–330°C, followed by a smaller peak at ~ 380 °C. These peaks are more overlapped for BiCit3-200. This suggests a multi-step decomposition pathway for $BiC_6H_5O_7$ in these samples, with at least two distinct thermal events. This observation contrasts with the single-step $BiC_6H_5O_7$ decomposition reported by Radecki and Wesołowski [19].

The DTG curves for BiCit1, BiCit2, and BiCit3-100 (Fig. 5c) also show a high degree of similarity above 250 °C, advocating a shared pathway for the decomposition of $BiC_6H_5O_7$, irrespective of the initial presence or absence of excess citric acid. A significant mass loss step is observed in the (D)TG curves (denoted as (2) in Fig. 5b) for BiCit1, BiCit2 and BiCit3-100, as well as BiCit3-200, at ~ 300 °C which aligns with the onset temperature of the more prominent exothermic peak in the DTA curve (Fig. 5a). Mass loss step (2) is closely followed by a much less significant mass loss process in the (D)TG curves at ~ 325 °C (denoted by (3) in the inset of Fig. 5b, c), although it is not as clearly evident for BiCit3-200. Mass loss step (3) aligns well with the end of the more prominent exothermic peak in the DTA curve (Fig. 5a). The final mass loss step occurs at ~ 375 °C and is most noticeable in the (D)TG curves of BiCit1-100 and BiCit3-100 (denoted (4) in Fig. 5b). Mass loss step (4) aligns well with the smaller, higher temperature exothermic peak in the DTA curve. The presence of these distinct mass loss steps on the (D)TG curves suggest a four-step thermal decomposition mechanism for $BiC_6H_5O_7$, which has not been reported before.

From the TG curve of BiCit1-100 (Fig. 5c), the residual mass is approximately 62.1 mass% at ~ 320 °C after mass loss step (2). Mansour [24] proposed a decomposition product mixture of Bi_2O_3, BiOAc, and BiO in a 1:1:1 molar ratio. Theoretically, this decomposition pathway would result in a residual mass of 58.6 mass%, which is notably lower than the value observed. The ambient XRD study of BiCit3-300 also did not indicate the presence of BiO in the decomposition products. Srivastava et al. [20] proposed an alternative decomposition pathway for $BiC_6H_5O_7$, leading to a mixture of Bi_2O_3 and BiOAc in a 1:3 molar ratio. While the ambient XRD study of BiCit3-300 confirms the presence of a two-phase mixture of Bi_2O_3 and BiOAc, the 1:3 molar ratio suggested by Srivastava et al. [20] would result in a theoretical residual mass of 79.2 mass%, which is significantly higher than the 62.1 mass% observed for BiCit1-100. In this work, we propose the decomposition pathway leading to the formation of a mixture of Bi_2O_3 and BiOAc ($BiOC_2H_3O_2$) in a 1:2 molar ratio which would give a theoretical residual mass of 62.1 mass%, assuming $BiC_6H_5O_7{\cdot}H_2O$ corresponds to 100 mass%. This decomposition pathway is described by Eq. (2):

$$4\,BiC_6H_5O_7(s) + 14\,O_2(g) \rightarrow Bi_2O_3(s) + 2\,BiOC_2H_3O_2(s) + 20\,CO_2(g) + 7\,H_2O\,(g) \quad (2)$$

The XRD study found ~ 7:3 mass ratio of Bi_2O_3 and BiOAc which translates to ~ 1.5:1 molar ratio (not 1:2) for BiCit3-300. This discrepancy is not unexpected since the sample was held at 300 °C for two hours allowing for significant conversion to the oxide, whereas for the thermal analysis BiCit1-100 was simply heated at 10 °C min^{-1} until 500 °C.

The distinct mass loss step (3) has not been previously reported in the literature for the thermal decomposition of $BiC_6H_5O_7$. At 375 °C, after mass loss step (3), the residual mass is 58.5 mass%. Although the decomposition pathway suggested by Mansour [24] (Bi_2O_3, BiOAc, and BiO in a 1:1:1 molar ratio) gives a residual mass close to this value (58.6 mass%), it was not considered since there is no evidence for the formation of BiO. The XRD study did, however, reveal the presence of $Bi_2O_2CO_3$ after annealing BiCit3 at 400 and 500 °C for 2 h respectively. This observation suggests that mass loss step (3) is associated with the complete decomposition of BiOAc resulting in the formation of $Bi_2O_2CO_3$, as shown in Eq. (3):

$$2\,BiOC_2H_3O_2(s) + 4\,O_2(g) \rightarrow Bi_2O_2CO_3(s) + 3\,CO_2(g) + 3\,H_2O\,(g) \quad (3)$$

The theoretical residual mass after the formation of $Bi_2O_2CO_3$ (from the decomposition of BiOAc) is 58.6 mass% (relative to four (4) moles of $BiC_6H_5O_7{\cdot}H_2O$) which is in excellent agreement with the experimental observation from the TG analysis (58.5 mass%).

The final mass loss step (4) is then due to the thermal decomposition of $Bi_2O_2CO_3$ leading to the formation of Bi_2O_3 as shown in Eq. (4):

$$Bi_2O_2CO_3(s) \rightarrow Bi_2O_3(s) + CO_2(g) \quad (4)$$

The overall thermal decomposition from room temperature is therefore described by Eq. (5):

$$4\,BiC_6H_5O_7 \cdot H_2O(s) + 18\,O_2(g) \rightarrow 2\,Bi_2O_3(s) + 24\,CO_2(g) + 11\,H_2O\,(g) \quad (5)$$

Conclusions

Literature presents contrasting findings regarding the thermal decomposition of $BiC_6H_5O_7$ to form Bi_2O_3. This study investigated the thermal decomposition of $BiC_6H_5O_7$ sol–gel precursors, synthesized using the citrate sol–gel method. Samples dried and annealed at different temperatures were analysed using ambient FTIR spectroscopy and XRD with Rietveld refinement, as well as the thermal analysis techniques TG, DTG and DTA. Our results confirm the complexation of Bi^{3+} by citric acid to form $BiC_6H_5O_7{\cdot}H_2O$ after drying at 100 °C. The initial step upon heating includes:

1. Dehydration (by ~ 150 °C) followed by the thermal decomposition of excess citric acid (~ 130–240 °C):

   $$BiC_6H_5O_7 \cdot H_2O + xC_6H_5O_7 \rightarrow BiC_6H_5O_7 + xC_6H_5O_7 \rightarrow BiC_6H_5O_7$$

   $BiC_6H_5O_7$ then decomposes to form Bi_2O_3 via the following steps (although O_2, CO_2 and H_2O have been omitted here for simplicity, the full balanced equations are presented in Eqs. 1–5):
2. Thermal decomposition of $BiC_6H_5O_7$ (~ 300 °C) according to the stoichiometric ratio:

   $$4\ BiC_6H_5O_7 \rightarrow Bi_2O_3 + 2\ BiOAc$$

   We also observed a potential direct $BiOAc \rightarrow Bi_2O_3$ decomposition reaction occurring during isothermal annealing at 300 °C according to the XRD results. The bismuth oxide acetate (BiOAc) then decomposed to form Bi_2O_3 via an intermediate subcarbonate phase:
3. Thermal decomposition of BiOAc (~ 325 °C):

   $$2\ BiOAc \rightarrow Bi_2O_2CO_3$$

4. Thermal decomposition of $Bi_2O_2CO_3$ (~ 375 °C):

   $$Bi_2O_2CO_3 \rightarrow Bi_2O_3$$

Steps (3) and (4), which involve the formation and decomposition of $Bi_2O_2CO_3$, confirmed by XRD and thermal analysis results, have not been previously reported. XRD results show that initially *orth*-$Bi_2O_2CO_3$ is formed, but *tetrag*-$Bi_2O_2CO_3$ is also formed after annealing at higher temperatures. It is possible that the exact synthetic route may influence the decomposition pathway of $BiC_6H_5O_7$ as it appears that residual carbon may be involved in $Bi_2O_2CO_3$ formation. The identification of this additional intermediate step in the phase transition to form Bi_2O_3 highlights the need for further investigation into the mechanism by which it occurs.

Supplementary Information The online version contains supplementary material available at https://doi.org/10.1007/s10973-025-14338-x.

Acknowledgements The authors hereby acknowledge the support of the National Research Foundation (NRF, South Africa, Grant No: 141966) and Department of Science and Innovation (DSI, South Africa, Grant UID: 41292) through the Centre of Excellence in Strong Materials (CoE-SM), as well as the University of the Witwatersrand towards this research. Opinions expressed and conclusions arrived at, are those of the authors and are not necessarily to be attributed to the NRF, DSI-NRF CoE-SM and/or the University of the Witwatersrand.

Author contributions DF: Conceptualization, Formal analysis and investigation, Writing—original draft preparation. CB: Conceptualization, Writing—review and editing, Supervision, Resources, Funding acquisition. DB: Conceptualization, Supervision, Resources, Funding acquisition.

Funding Open access funding provided by University of the Witwatersrand.

Data availability The data that support the findings of this study are available from the corresponding author, Caren Billing, upon reasonable request.

Declarations

Conflict of interest All authors declare no conflict of interest, financial or otherwise, related to the research and findings presented in this manuscript.

References

1. Reverberi AP, Varbanov PS, Vocciante M, Fabiano B. Bismuth oxide-related photocatalysts in green nanotechnology: a critical analysis. Front Chem Sci Eng. 2018;12(4):878–92. https://doi.org/10.1007/s11705-018-1744-5.
2. Mane V, Dake D, Raskar N, Sonpir R, Stathatos E, Dole B. A review on Bi_2O_3 nanomaterial for photocatalytic and antibacterial applications. Chem Phys Impact. 2024;8: 100517. https://doi.org/10.1016/j.chphi.2024.100517.
3. Ghuge RS, Shinde MD, Rane SB. Bismuth-based gas sensors: a comprehensive review. J Electron Mater. 2021;50(11):6060–72. https://doi.org/10.1007/s11664-021-09174-2.
4. Ge L, Mu X, Tian G, Huang Q, Ahmed J, Hu Z. Current applications of gas sensor based on 2-D nanomaterial: a mini review. Front Chem. 2019;7:839. https://doi.org/10.3389/fchem.2019.00839.

5. Azad AM, Larose S, Akbar SA. Bismuth oxide-based solid electrolytes for fuel cells. J Mater Sci. 1994;29(16):4135–51. https://doi.org/10.1007/BF00414192.
6. Shuk P, Wiemhöfer HD, Guth U, Göpel W, Greenblatt M. Oxide ion conducting solid electrolytes based on Bi_2O_3. Solid State Ion. 1996;89:179–96. https://doi.org/10.1016/0167-2738(96)00348-7.
7. Sammes NM, Tompsett GA, Näfe H, Aldinger F. Bismuth based oxide electrolytes—structure and ionic conductivity. J Eur Ceram Soc. 1999;19(10):1801–26. https://doi.org/10.1016/S0955-2219(99)00009-6.
8. Drache M, Roussel P, Wignacourt JP. Structures and oxide mobility in Bi-Ln-O materials: heritage of Bi_2O_3. Chem Rev. 2007;107(1):80–96. https://doi.org/10.1021/cr050977s.
9. Harwig HA. On the structure of bismuthsesquioxide: the α, β, γ, and δ-phase. Z Anorg Allg Chem. 1978;444:151–66. https://doi.org/10.1002/zaac.19784440118.
10. Levin EM, Roth RS. Polymorphism of bismuth sesquioxide. I. Pure Bi_2O_3. J Res Natl Bur Stand Sect Phys Chem. 1964;68(2):189–95. https://doi.org/10.6028/jres.068A.019.
11. Iyyapushpam S, Nishanthi ST, Pathinettam PD. Photocatalytic degradation of methyl orange using α-Bi_2O_3 prepared without surfactant. J Alloys Compd. 2013;563:104–7. https://doi.org/10.1016/j.jallcom.2013.02.107.
12. Sood S, Umar A, Kumar Mehta S, Kumar KS. α-Bi_2O_3 nanorods: an efficient sunlight active photocatalyst for degradation of rhodamine B and 2,4,6-trichlorophenol. Ceram Int. 2015;41(3):3355–64. https://doi.org/10.1016/j.ceramint.2014.10.038.
13. Blower SK, Greaves C. The structure of β-Bi_2O_3 from powder neutron diffraction data. Acta Crystallogr C. 1988;44:587–9. https://doi.org/10.1107/S0108270187011661.
14. Zahid AH, Han Q. A review on the preparation, microstructure, and photocatalytic performance of Bi_2O_3 in polymorphs. Nanoscale. 2021;13(42):17687–724. https://doi.org/10.1039/D1NR03187B.
15. Jalalah M, Faisal M, Bouzid H, Park J-G, Al-Sayari SA, Ismail AA. Comparative study on photocatalytic performances of crystalline α- and β-Bi_2O_3 nanoparticles under visible light. J Ind Eng Chem. 2015;30:183–9. https://doi.org/10.1016/j.jiec.2015.05.020.
16. Selvamani T, Anandan S, Granone L, Bahnemann DW, Ashokkumar M. Phase-controlled synthesis of bismuth oxide polymorphs for photocatalytic applications. Mater Chem Front. 2018;2(9):1664–73. https://doi.org/10.1039/C8QM00221E.
17. Iyyapushpam S, Nishanthi ST, Pathinettam PD. Enhanced photocatalytic degradation of methyl orange by gamma Bi_2O_3 and its kinetics. J Alloys Compd. 2014;601:85–7. https://doi.org/10.1016/j.jallcom.2014.02.142.
18. Danks AE, Hall SR, Schnepp Z. The evolution of "sol–gel" chemistry as a technique for materials synthesis. Mater Horiz. 2016;3(2):91–112. https://doi.org/10.1039/c5mh00260e.
19. Radecki A, Wesołowski M. The thermal decomposition of bismuth(III) compounds used in medicine. Thermochim Acta. 1976;17:217–29. https://doi.org/10.1016/0040-6031(76)85028-9.
20. Srivastava A, Gunjikar VG, Sinha APB. Thermoanalytical studies of zinc citrate, bismuth citrate and calcium citrate. Thermochim Acta. 1987;117:201–17. https://doi.org/10.1016/0040-6031(87)88115-7.
21. Anilkumar M, Pasricha R, Ravi V. Synthesis of bismuth oxide nanoparticles by citrate gel method. Ceram Int. 2005;31(6):889–91. https://doi.org/10.1016/j.ceramint.2004.09.002.
22. Astuti Y, Listyani BM, Suyati L, Darmawan A. Bismuth oxide prepared by sol–gel method: variation of physicochemical characteristics and photocatalytic activity due to difference in calcination temperature. Indones J Chem. 2021;21(1):108–17. https://doi.org/10.22146/ijc.53144.
23. Astuti Y, Nurhayati S, Arnelli. Effect of calcination temperature on the morphology and photocatalytic activity of bismuth oxide. AIP Conf Proc. 2022. https://doi.org/10.1063/5.0104124.
24. Mansour SAA. Thermal decomposition of anhydrous bismuth citrate. Thermochim Acta. 1994;233(2):257–68. https://doi.org/10.1016/0040-6031(94)85119-0.
25. Yang N, Sun H. Biocoordination chemistry of bismuth: recent advances. Coord Chem Rev. 2007;251(17–20):2354–66. https://doi.org/10.1016/j.ccr.2007.03.003.
26. Ge R, Chen Z, Zhou Q. The actions of bismuth in the treatment of *Helicobacter pylori* infections: an update. Metallomics. 2012;4(3):239. https://doi.org/10.1039/c2mt00180b.
27. Rietveld HM. A profile refinement method for nuclear and magnetic structures. J Appl Crystallogr. 1969;2(2):65–71. https://doi.org/10.1107/S0021889869006558.
28. Haynes WM, Lido DR, Bruno TJ. CRC handbook of chemistry and physics: a ready-reference book of chemical and physical data. 95th ed. Boca Raton: CRC Press; 2014.
29. Gill WE. Determination of NO_2 and NO in air. Am Ind Hyg Assoc J. 1960;21(1):87–96. https://doi.org/10.1080/00028896009343313.
30. Dinnebier RE, Leineweber A, Evans JSO. Rietveld refinement: practical powder diffraction pattern analysis using TOPAS. Berlin: De Gruyter; 2019.
31. Wieser ME, Holden N, Coplen TB, Böhlke JK, Berglund M, Brand WA, De Bièvre P, Gröning M, Loss RD, Meija J, Hirata T, Prohaska T, Schoenberg R, O'Connor G, Walczyk T, Yoneda S, Zhu X-K. Atomic weights of the elements 2011 (IUPAC technical report). Pure Appl Chem. 2013;85(5):1047–78. https://doi.org/10.1351/PAC-REP-13-03-02.
32. Lafontaine A, Sanselme M, Cartigny Y, Cardinael P, Coquerel G. Characterization of the transition between the monohydrate and the anhydrous citric acid. J Therm Anal Calorim. 2013;112(1):307–15. https://doi.org/10.1007/s10973-012-2798-0.
33. Sadler PJ, Li H, Sun H. Coordination chemistry of metals in medicine: target sites for bismuth. Coord Chem Rev. 1999;185–186:689–709. https://doi.org/10.1016/S0010-8545(99)00018-1.
34. Brown PJ, Fox AG, Maslen EN, O'Keefe MA, Willis BTM. Intensity of diffracted intensities. In: Fuess H, Hahn T, Wondratschek H, Müller U, Shmueli U, Prince E, Authier A, Kopský V, Litvin DB, Rossmann MG, Arnold E, Hall S, McMahon B, editors. International tables for crystallography, vol. C. Chester: International Union of Crystallography; 2006. p. 554–95. https://doi.org/10.1107/97809553602060000600.
35. Poerwono H, Higashiyama K, Kubo H, Poernomo AT, Suharjono I, Sudiana IK, Indrayanto G, Brittain HG. Citric acid. Anal Profiles Drug Subst Excip. 2001;28:1–76. https://doi.org/10.1016/S1075-6280(01)28002-1.
36. Stuart BH. Infrared spectroscopy: fundamentals and applications; analytical techniques in the sciences. Hoboken: Wiley; 2004.
37. Smith BC. Infrared spectral interpretation: a systematic approach. Boca Raton: CRC Press; 1999.
38. Aurivillius B, Gloor U. X-ray studies on bismuth oxide acetate $CH_3COO{\cdot}OBi$ and related compounds. Acta Chem Scand. 1955;9:1213–8.
39. Sillen L. X-ray studies on BiOCl, BiOBr and BiOI. Sven Kem Tidsk. 1941;53:39–43.
40. Shannon RD, Prewitt CT. Effective ionic radii in oxides and fluorides. Acta Crystallogr B. 1969;25(5):925–46. https://doi.org/10.1107/s0567740869003220.

41. Shannon RD, Prewitt CT. Revised values of effective ionic radii. Acta Crystallogr B. 1970;26(7):1046–8. https://doi.org/10.1107/s0567740870003576.
42. Grice JD. A solution to the crystal structures of bismutite and beyerite. Can Miner. 2002;40:693–8. https://doi.org/10.2113/gscanmin.40.2.693.
43. Lagercrantz A, Sillen LG. On the crystal structure of $Bi_2O_2CO_3$ (bismutite) and $CaBi_2O_2(CO_3)_2$ (beyerite). Stockholm: Almqvist & Wiksell; 1948.
44. Barbooti MM, Al-Sammerrai DA. Thermal decomposition of citric acid. Thermochim Acta. 1986;98:119–26. https://doi.org/10.1016/0040-6031(86)87081-2.
45. Li H, Jiang P, Zhang J, Luo X, Long Z. An one-pot approach to hierarchical flower-like $Bi_2O_2CO_3/Bi_2WO_6$ heterojunctions: self-assembly, in situ carbonization, and enhanced visible light photocatalytic activities. Mater Express. 2021;11(4):533–9. https://doi.org/10.1166/mex.2021.1934.
46. Carlson WD. The polymorphs of $CaCO_3$ and the aragonite-calcite transformation. Rev Miner. 1983;11:191–225.
47. Wiecinska P. Thermal degradation of organic additives used in colloidal shaping of ceramics investigated by the coupled DTA/TG/MS analysis. J Therm Anal Calorim. 2016;123:1419–30. https://doi.org/10.1007/s10973-015-5075-1.